

# Peculiar band geometry induced giant shift current in ferroelectric SnTe monolayer

Gan Jin<sup>1</sup> and Lixin He<sup>1,2,\*</sup>

<sup>1</sup>*Key Laboratory of Quantum Information, University of Science and Technology of China, Hefei, Anhui, 230026, People's Republic of China*

<sup>2</sup>*Institute of Artificial Intelligence, Hefei Comprehensive National Science Center, Hefei, Anhui, 230026, People's Republic of China*

The bulk photovoltaic effect (BPVE) refers to the phenomenon of generating photocurrent or photovoltage in homogeneous noncentrosymmetric materials under illumination, and the intrinsic contribution to the BPVE is known as the shift current effect. We calculate the shift current conductivities of the ferroelectric SnTe monolayer using first-principles methods. We find that the monolayer SnTe has giant shift-current conductivity near the valley points. More remarkably, the linear optical absorption coefficient at this energy is very small, and therefore leads to an enormous Glass coefficient that is four orders of magnitude larger than that of BaTiO<sub>3</sub>. The unusual shift-current effects are further investigated using a three-band model. We find that the giant shift current conductivities and Glass coefficient are induced by the nontrivial energy band geometries near the valley points, where the shift-vector diverges. This is a prominent example that the band geometry can play essential roles in the fundamental properties of solids.

## INTRODUCTION

The study of BPVE has a long history [1–3], and recently it has attracted great renewed interest because it potentially allows the energy conversion efficiency to surpass the Shockley–Queisser limit [4, 5]. The shift-current effects are believed to be the main intrinsic contribution to the BPVE [3, 6], which can be used as an alternative to the photocurrent generated by traditional semiconductor p–n junctions [7, 8]. It has been demonstrated that the photovoltage generated by shift-current effects can be far above the band gap [9–12].

The high priority of current studies in the field is to find novel materials that have high shift-current conductivities. Cook et al. proposed design principles of the shift current materials through an effective two-dimensional model and successfully applied them to monochalcogenide GeS [8]. In addition to conventional ferroelectric materials [13, 14], special attention has been given to Weyl semimetals because of the unique topological nature of band structures. Osterhoudt et al. discovered a huge mid-infrared BPVE in the Weyl semimetal TaAs, which is linked to the topological properties of the material [15]. Type-II Weyl semimetal TaIrTe<sub>4</sub> has been found to have a huge optical response, and the shift current is related to the divergent Berry curvature at the Weyl nodes [16]. Ahn et al. theoretically studied the low-frequency properties of BPVEs in topological semimetals, and revealed the relation between the shift current as well as the injection current and the quantum geometry of the material near the Weyl point [17].

In this work, we investigate the nonlinear optical properties of the two-dimensional ferroelectric material SnTe monolayer [18] using first-principles methods. We find that it has giant shift current conductivities near the valley points. More remarkably, the linear optical absorption coefficient at this energy is very small, which leads to an enormous Glass coefficient of four orders of magnitude larger than that of bulk BaTiO<sub>3</sub> [1, 5, 19].

We develop a minimal three-band model to analyze the mechanism of the giant shift-current effect in the SnTe monolayer. We find that the giant shift-current effects are induced by the nontrivial band structure geometry, where the shift-vector diverges at the valley point. We further show that the giant shift-current is related to the derivatives of the imaginary part of the quantum geometric tensor near the point. The mechanism is different from the previous works on the Weyl semimetals [17], and therefore opens a new play ground for the fascinating physical properties that are determined by the band structure geometries.

## RESULTS

### Crystal structure

In 2016, Chang et al. [18] discovered that the SnTe monolayer has robust in-plane ferroelectricity with a Curie temperature as high as 270 K, which is greatly enhanced from its bulk value of 98 K. As a member of the Group IV monochalcogenide (MX, M = Ge, Sn, Pb; X = S, Se, Te) family, the SnTe monolayer, which has great potential in miniaturized ferroelectric devices, has been extensively studied experimentally [20] and via first-principles calculations [21–23]. The structure of the SnTe monolayer is shown in Fig. 1, which has a hinge-like structure similar to that of phosphorene. The SnTe monolayer has a Pmn2<sub>1</sub> space group with mirror symmetry ( $M_{xz}$ ) and glide mirror symmetry ( $G$ ). It has an in-plane ferroelectricity along the  $x$ -axis [20–23].

The lack of inversion symmetry suggests that the SnTe monolayer should have shift-current effects. We perform first-principles calculations to investigate the shift-current effects in the SnTe monolayer. Details of the calculations are presented in the METHODS section.

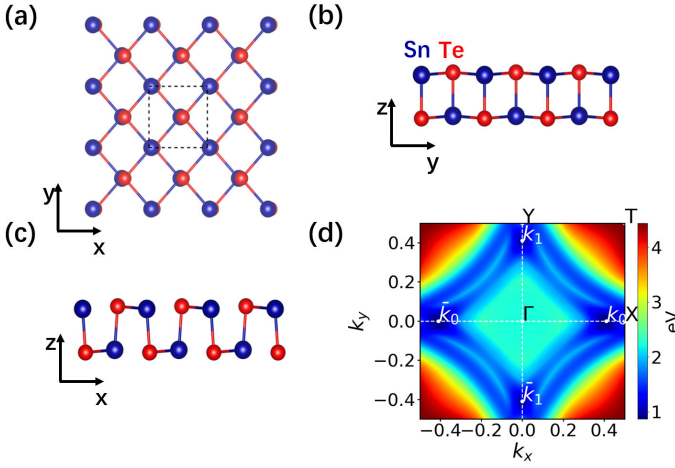


FIG. 1. (a) Top view, (b) side view along the  $x$  direction and (c) side view along the  $y$  direction of the crystal structure of the SnTe monolayer. Sn and Te atoms are shown using blue and red spheres, respectively. The unit cell is indicated by the dashed rectangle in (a). (d) The band gap between the lowest conduction band and the highest valence band in the Brillouin zone, where  $\mathbf{k}_0$ ,  $\mathbf{k}_1$  and  $\mathbf{k}_2$  are the valley points.

### Band structure and shift current conductivities

The band structures of SnTe monolayer with and without spin-orbit coupling (SOC) are shown in Fig. S1 of the Supplementary Information (SI). There are four valley points of the band structure in the first Brillouin zone. Two valley points,  $\mathbf{k}_0=(0.41, 0.0)$ ,  $\mathbf{k}_1=(0.0, 0.41)$ , in direct coordinates, are on the  $\Gamma$ - $X$  line and  $\Gamma$ - $Y$  line respectively, whereas the other two valley points are obtained by the time inversion symmetry of the above two  $k$ -points, i.e.,  $\bar{\mathbf{k}}_0 = -\mathbf{k}_0$  and  $\bar{\mathbf{k}}_1 = -\mathbf{k}_1$ , as shown in Fig. 1(d). The introduction of SOC only slightly changes the positions of the valley points (see Fig. S1 in SI).

The break of inversion symmetry would lead to the shift current in the SnTe monolayer, i.e., a nonlinear dc photocurrent under illumination [1–3],

$$J^a = 2\sigma^{abc}(0; \omega, -\omega)E_b(\omega)E_c(-\omega), \quad (1)$$

where  $\sigma^{abc}(0; \omega, -\omega)$  is the shift-current conductivity, and  $a$  ( $b, c$ )= $x, y, z$  are the crystal axes. Due to the 2D monolayer structure, we do not consider the current in the  $z$ -direction. Similarly, we do not consider the electric field applied in the  $z$ -direction. Because of the mirror symmetry  $M_{xz}$  of the SnTe monolayer, only  $\sigma^{xxx}$ ,  $\sigma^{xyy}$ , and  $\sigma^{yxy}=\sigma^{yyx}$  are nonzero (see the SI).

We investigate the shift-current conductivities by using first-principles calculations [3, 24–26], and the numerical results are consistent with the above symmetry analysis. The 3D-like conductivities are obtained assuming an active single-layer thickness of 3.12 Å [25, 27]. Although quantitatively, the results with and without SOC are somehow different, but the inclusion of SOC does not affect the main results and conclusions of the paper

(see Fig. S4 in SI). Therefore, we only discuss the results without SOC here, and the analysis can be equally applied to the results with SOC.

Figure 2(a) depicts  $\sigma^{yxy}$ , which is the largest component of the shift-current conductivities.  $\sigma^{yxy}$  has three distinct peaks at 0.87 eV, 1.24 eV, and 2.18 eV, respectively, in the energy interval 0~4 eV. The highest peak is at  $\hbar\omega_0=0.87$  eV, with  $\sigma_{3D}^{yxy}=481.89 \mu\text{A}/\text{V}^2$ , which is significantly larger than the known high BPVE material GeS of the order of  $150 \mu\text{A}/\text{V}^2$  and  $250 \mu\text{A}/\text{V}^2$  in state-of-the-art Si-based solar cells [25, 27, 28].

To experimentally explore this effect, we may apply light with an electric field polarized along the  $[110]$  direction, and measure the shift current along the  $y$  direction, which gives

$$j^y = 2\sigma^{yxy}E_x(\omega)E_y(-\omega). \quad (2)$$

In previous works [7, 8, 25], it has been suggested that to have a large shift current, a large joint density of states (JDOS) is necessary, which has been used as a design principle in finding materials with a large shift current. Surprisingly, we find that the JDOS at  $\hbar\omega_0=0.87$  eV is extremely small as plotted in Fig. S2 in the SI. As a consequence, the absorption coefficients are expected to be small at this photon energy. Indeed, the absorption coefficient  $\alpha^{[110]}$  is also very small around  $\hbar\omega_0=0.87$  eV, as shown in Fig. 2(b). What is more amazing is that the absorption coefficient  $\alpha^{yy}=0$  at this energy, strongly against our intuition, given that  $\sigma^{yxy}$  is huge.

The above results have important physical consequences. We compute the Glass coefficient [1, 7, 9, 24]

$$g^{abc} = \alpha^{-1}\sigma^{abc}, \quad (3)$$

and the result of  $g^{yxy}$  is shown in Fig. 2(c).  $g^{yxy}$  has a sharp peak at  $\hbar\omega_0=0.87$  eV, due to the giant  $\sigma^{yxy}$  and small  $\alpha^{[110]}$ . The calculated Glass coefficient  $g^{yxy}$  of the SnTe monolayer at  $\hbar\omega_0=0.87$  eV is  $5.2 \times 10^{-5} \text{ cm}\cdot\text{V}^{-1}$  [27], which is four orders of magnitude higher than  $g_{31}=3 \times 10^{-9} \text{ cm}\cdot\text{V}^{-1}$  of the bulk (001)-oriented BaTiO<sub>3</sub> crystal [1, 5, 19]. The Glass coefficient  $g$  plays essential roles in the shift current related physical properties. For example, the photovoltaic field generated by the shift current [1, 5] can be estimated as,

$$E_{\text{pv}} \approx \frac{g}{\phi(\mu\tau)_{\text{pv}}} \frac{\hbar\omega}{e}, \quad (4)$$

where  $\phi$  is the quantum yield,  $\hbar\omega$  is the incident photon energy and  $\mu$  and  $\tau$  are the mobility and lifetime of the carriers responsible for photoconductivity. A very large  $g$  will lead to a very large photovoltaic field  $E_{\text{pv}}$ , as in this case, the “leaking” current due to photoconductivity is much weaker than the shift current. The photovoltaic power conversion efficiency is also closely related to the Glass coefficient [1].

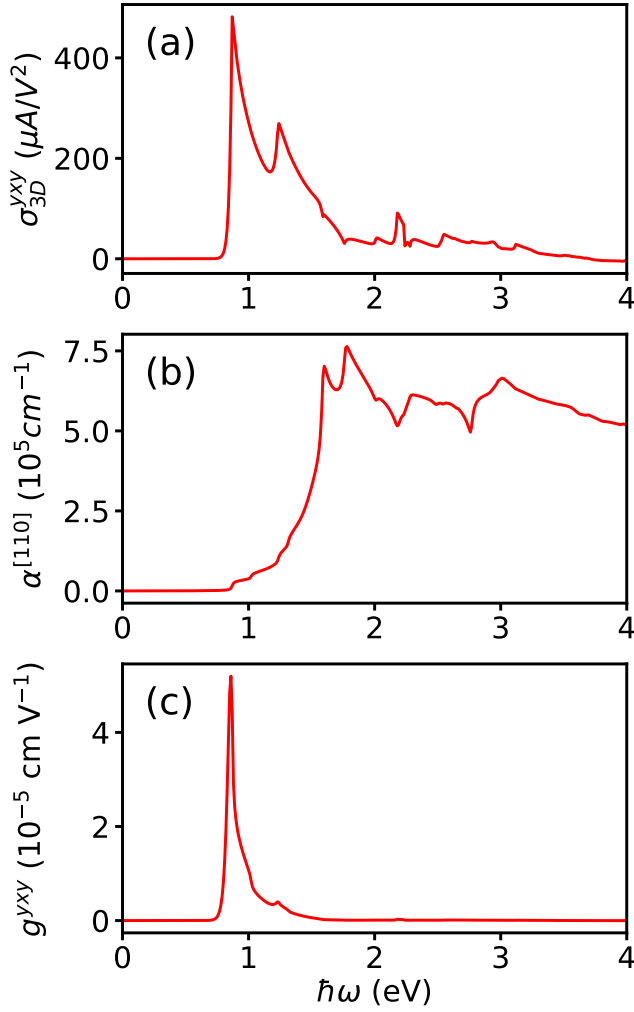


FIG. 2. (a) Shift current conductivity  $\sigma_{3D}^{xy}$  of the SnTe monolayer. There are three peaks at 0.87, 1.24, and 2.18 eV, respectively. The highest peak is at 0.87 eV. (b) The absorption coefficient  $\alpha^{[110]}$  and (c) the Glass coefficient of the SnTe monolayer, respectively. The Glass coefficient has a sharp peak at 0.87 eV.

## DISCUSSION

### Origin of the giant shift current in $xy$ direction

It is particularly interesting and important to explore the underlying mechanism of the giant shift-current conductivity and Glass coefficient in the SnTe monolayer. The shift-current tensor is given by [3],

$$\sigma^{abc}(0; \omega, -\omega) = \frac{\pi e^3}{\hbar^2} \int \frac{d\mathbf{k}}{8\pi^3} \sum_{n,m} f_{nm} \text{Im} [I_{mn}^{abc} + I_{mn}^{acb}] \delta(\omega_{mn} - \omega), \quad (5)$$

where  $f_{nm} = f_n - f_m$  and  $\hbar\omega_{nm} = E_m - E_n$  are differences between Fermi occupation factors and band energies, re-

spectively.  $I_{mn}^{abc} = r_{mn}^b r_{nm;a}^c$ , where  $r_{nm}^a$  is the inter-band dipole matrix, and  $r_{nm;a}^b$  is the generalized derivative of the dipole matrix, i.e.,

$$r_{nm}^a = (1 - \delta_{nm}) A_{nm}^a, \quad (6)$$

$$r_{nm;b}^a = \partial_b r_{nm}^a - i(A_{nn}^b - A_{mm}^b) r_{nm}^a. \quad (7)$$

Here,  $A_{nm}^a$  is the non-Abelian Berry connection. More detailed calculations of  $r_{nm}^a$  and  $r_{nm;b}^a$  are described in Methods. Although  $r_{nm}^a$  and  $r_{nm;a}^b$  are gauge dependent, their norm  $|r_{nm}^a|$  and  $|r_{nm;a}^b|$ , as well as  $I_{mn}^{abc}$  are gauge invariant [25]. Note that  $r_{nm}^a$  and  $r_{nm;a}^b$  and  $I_{mn}^{abc}$  are all  $\mathbf{k}$  dependent, but here we drop the  $\mathbf{k}$  index for simplicity.

We calculate  $\sum_{n,m} f_{nm} \text{Im} [I_{mn}^{xy} + I_{mn}^{yyx}] \delta(\omega_{mn} - \omega_0)$ , for  $\hbar\omega_0 = 0.87$  eV, in the first BZ [see Fig. S3(a) of SI]. We find the contribution solely comes from the transition between the highest valence band and the lowest conduction band, around the valley points  $\mathbf{k}_0$  and  $\bar{\mathbf{k}}_0$ . Because only the valley points contribute to the optical transitions at  $\hbar\omega_0$ , the corresponding JDOS and linear absorption coefficient is very small. Furthermore, as shown in Fig. S3(b) of SI,  $I_{vc} = \text{Im} [I_{vc}^{xy} + I_{vc}^{yyx}]$ , where  $v$  and  $c$ , are the highest valence band and the lowest conduction band, has a sharp peak at  $\mathbf{k}_0$ , which leads to the giant shift-current conductivity.

Figure 3(a) depicts the norm of  $r_{vc}^x$  and  $r_{vc}^y$  along  $k_y$  passing through  $\mathbf{k}_0$ , which are shown in red and blue solid lines respectively. We see  $|r_{vc}^x|$  has a maximum at  $k_y = 0$ , whereas  $|r_{vc}^y| = 0$  at  $\mathbf{k}_0$  due to the mirror symmetry  $M_{xz}$ . However, as seen from Fig. 3(a),  $|r_{vc}^y|$  changes rapidly along  $k_y$  around  $\mathbf{k}_0$ . One may speculate that  $r_{vc}^y$  may have a large partial derivative (Eq. 7) along  $k_y$  at the valley point. Indeed, as shown in Fig. 3(b),  $|r_{cv;y}^y|$  has a peak at  $\mathbf{k}_0$ . We plot  $I_{vc}$  in Fig. 3(c). Interestingly, we find that  $I_{vc} \approx |r_{vc}^x| |r_{vc;y}^y|$  around  $\mathbf{k}_0$  (See SI). Both  $r_{vc}^x$  and  $r_{cv;y}^y$  reach the maximum at  $\mathbf{k}_0$ , which lead to the giant  $I_{vc}$ .

### Three-band model

To gain a deeper insight into the physics, we construct a minimal three-band model around the valley point  $\mathbf{k}_0$ ,

$$H(\mathbf{k}) = H_0 + \mathbb{A} \delta k_x + \mathbb{B} \delta k_y + \mathbb{C} \delta k_x^2 + \mathbb{D} \delta k_x \delta k_y + \mathbb{E} \delta k_y^2, \quad (8)$$

up to the quadratic terms of  $\delta \mathbf{k}$ , where  $\delta \mathbf{k} = \mathbf{k} - \mathbf{k}_0$ . More specifically,  $\delta k_x = k_x - 0.41$ ,  $\delta k_y = k_y$ . We therefore do not distinguish  $k_y$  and  $\delta k_y$  below. In the model, the 1st-band is the highest valence band, whereas the 2nd-band and 3rd-band correspond to the lowest two conduction bands in the DFT calculations. We fit the Hamiltonian matrix  $H(\mathbf{k})$  and velocity matrix  $v_{mn}(\mathbf{k})$  from DFT calculations around  $\mathbf{k}_0$ . The fitted parameters of the model are given in the SI.

We first (numerically) calculate  $|r_{12}^x|$ ,  $|r_{12;y}^y|$ , and  $I_{12}$  of the three-band model, and the results are compared with those of DFT calculations in Fig. 3(a),(b),

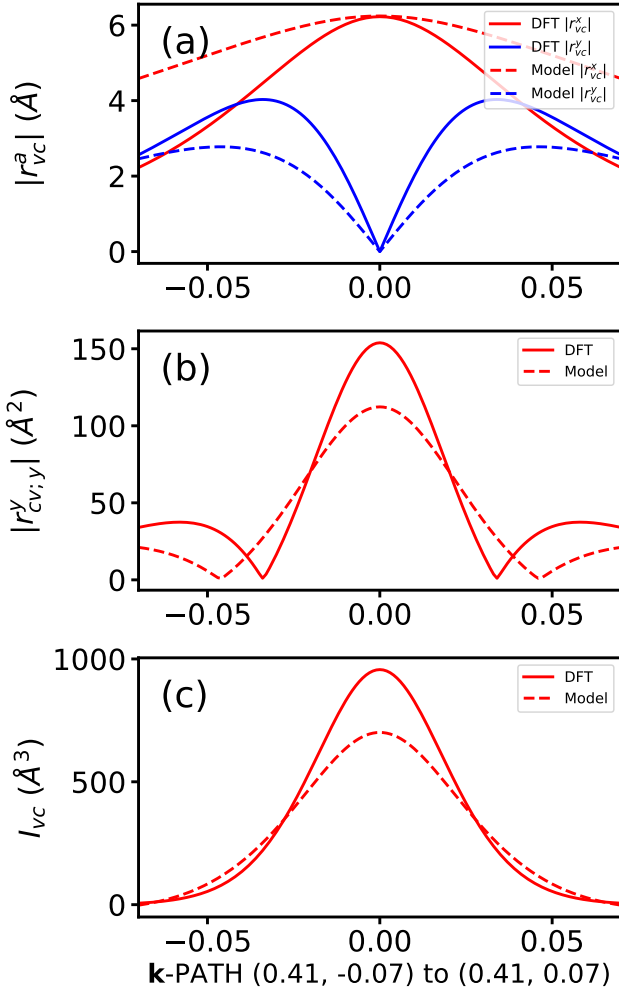


FIG. 3. (a) The norm of dipole matrix  $r^x_{vc}$  and  $r^y_{vc}$  along  $k_y$ , where  $v$  and  $c$  are highest valence band and lowest conduction band, respectively. (b) The norm of the generalized derivative of dipole matrix,  $r^x_{cv;y}$ , along  $k_y$ . (d) The  $I_{vc} = \text{Im}[I^{yx}_{vc} + I^{xy}_{vc}]$  along  $k_y$ . The results obtained from DFT and model calculations are shown in solid and dashed lines, respectively.

and (c), respectively. The three-band model can semi-quantitatively reproduce the results of DFT calculations, and the discrepancies are due to neglecting other bands.

Around  $\mathbf{k}_0$ , the wave functions of the three-band model can be solved analytically via a second order perturbation theory, and therefore  $r^a_{nm}$  and  $r^a_{nm;b}$  can also be calculated analytically. Especially, at  $\mathbf{k}_0$  we have  $v^x_{nm}(\mathbf{k}_0) = \mathbb{A}_{nm}$  and  $v^y_{nm}(\mathbf{k}_0) = \mathbb{B}_{nm}$ , therefore

$$r^x_{nm}(\mathbf{k}_0) = \frac{\mathbb{A}_{nm}}{i\omega_{nm}}, \quad r^y_{nm}(\mathbf{k}_0) = \frac{\mathbb{B}_{nm}}{i\omega_{nm}}. \quad (9)$$

Because  $\mathbb{A}_{12} \neq 0$ , and  $\mathbb{B}_{12} = 0$ , which is actually imposed by the mirror symmetry, we have  $r^x_{12}(\mathbf{k}_0) \neq 0$ , but  $r^y_{12}(\mathbf{k}_0) = 0$ . This means that the linear (or direct) optical transition between the 1st and 2nd bands along  $k_y$  is forbidden. Similarly we calculate the  $r^b_{nm;a}$  of the valley

point  $\mathbf{k}_0$  [see Eq. (S14) in SI], and we have,

$$r^y_{21;y}(\mathbf{k}_0) = \frac{i}{\omega_{21}} \left[ \mathbb{B}_{23}\mathbb{B}_{31} \left( \frac{1}{\omega_{31}} + \frac{1}{\omega_{32}} \right) - 2\mathbb{E}_{21} \right]. \quad (10)$$

In the model, the value of  $r^y_{21;y}$  (and therefore  $I^{yx}_{12}$ ) depends mainly on the virtual transitions,  $\mathbb{B}_{23}\mathbb{B}_{31}$ , which corresponding to the last term in Eq. 20. The first term in Eq. 20 vanishes, because  $\mathbb{B}_{12} = 0$ . This is remarkable that the linear (direct) optical transition between the 1st-band and the 2nd-band in the  $y$  direction is forbidden, but the nonlinear transition may occur because both the 1st-band and 2nd-band have strong coupling with the 3rd-band, which leads to the giant shift-current effect. This effect is quite different from that of the two-band models for Weyl semimetals [17].

The giant shift-current effects have even more profound origins. An alternative expression for the shift-current conductivity is written as [17],

$$\sigma^{yxy} = -\frac{\pi e^3}{\hbar^2} \int_{\mathbf{k}} \sum_{n,m} f_{nm} (R^{y_{mn;y}} - R^{x_{nm;y}}) r^x_{nm} r^y_{mn} \delta(\omega_{mn} - \omega), \quad (11)$$

where,

$$R^b_{mn;a} = i\partial_a \ln r^b_{mn} + A^a_{mm} - A^a_{nn}, \quad (12)$$

is known as the shift vector, which characterizes the displacement of electrons in real space during the inter-band transition [1, 29, 30]. The shift vector is a gauge invariant quantity and can be viewed as a quantum geometric potential [31]. According to the perturbation theory, near  $\mathbf{k}_0$ ,  $r^y_{12}(\mathbf{k}) = f_4 k_y + f_5 \delta k_x k_y$ , where  $f_4$  and  $f_5$  are constants. In the model,  $A^a_{11}(\mathbf{k}_0) = 0$  and  $A^a_{22}(\mathbf{k}_0) = 0$  at  $\mathbf{k}_0$ , and both are small around  $\mathbf{k}_0$ . We can therefore neglect them in the following calculations. As  $\mathbf{k}$  approaches  $\mathbf{k}_0$  along  $k_y$ , i.e.,  $\delta k_x = 0$ , we have,

$$R^y_{12;y} = i\partial_y \ln(f_4 k_y) = \frac{i}{k_y}, \quad (13)$$

i.e.,  $R^y_{12;y}$  is purely imaginary and goes to infinity. Therefore,  $\mathbf{k}_0$  is a singular point for the shift vector  $R^y_{12;y}$ , which is a monopole in  $k$ -space. When  $k_y$  is approaching zero,  $r^y_{12}$  is also approaching zero as discussed in previous sections, and  $R^x_{21;y} r^x_{21} r^y_{12}$  vanishes, but  $R^y_{12;y} r^x_{21} r^y_{12}$  is still finite (actually very large) and purely real (see Fig. 3). The shift vectors also play important roles in second harmonic generation [17, 32, 33]. It is therefore expected that the SnTe monolayer would have non-trivial second harmonic responses. The divergent of the shift vector at the “optical zero” (i.e.,  $r_{cv} = 0$ ) was discussed in Ref. [34]. However, the relation between the giant shift current and the divergent shift vector is not revealed.

Very recently, nonlinear optical transitions have been related to the Riemannian geometry of the energy bands [17, 35]. We may define the quantum geometric tensor

between two bands  $m$  and  $n$ ,

$$Q_{ba}^{mn} = r_{nm}^b r_{mn}^a \equiv g_{ba}^{mn} - \frac{i}{2} F_{ba}^{mn}, \quad a, b = x, y, z \quad (14)$$

where  $g_{ba}^{mn}$  is the band-resolved quantum metric,  $F_{ba}^{mn}$  is the band-resolved Berry curvature, and the two geometric quantities are related to U(1) quantum metric and Berry curvature as  $g_{ba}^n = \sum_{m \neq n} g_{ba}^{mn}$  and  $\Omega_c^n = \sum_{m \neq n} \epsilon_{cba} F_{ba}^{mn} / 2$  [36, 37].

In our case, we consider the transition between the 1st band and the 2nd band, and the quantum geometric tensor of the two bands is given by  $Q_{xy}^{12} = r_{12}^x r_{21}^y$ . We have  $Q_{xy}^{12}(\mathbf{k}_0) = 0$  because  $r_{21}^y(\mathbf{k}_0) = 0$ . However, we show that the partial derivative of the imaginary part of  $Q_{xy}^{12}$  is related to  $I_{12}^{yxy}$ , i.e.,

$$\text{Im}[I_{12}^{yxy}(\mathbf{k}_0)] = \partial_y \text{Im}[Q_{xy}^{12}]|_{\mathbf{k}=\mathbf{k}_0} = -\frac{1}{2} \partial_y F_{xy}^{12}|_{\mathbf{k}=\mathbf{k}_0}. \quad (15)$$

Figure 4(a) illustrates the distribution of  $\text{Im}[Q_{xy}^{12}]$  near  $\mathbf{k}_0$  and its derivative with respect to  $k_y$  is shown in Fig. 4(b).  $\text{Im}[Q_{xy}^{12}]$  has a maximum (minimum) at  $\delta k_y = 0.05$  ( $\delta k_y = -0.05$ ) and  $\delta k_x = 0$ , which is very similar to the Berry curvature distribution in Fig. 2a of Ref. [23]. Furthermore,  $\text{Im}[Q_{xy}^{12}]$  changes rapidly around  $\delta k_y = 0$ , and as a consequence,  $\text{Im}[I_{12}^{yxy}(\mathbf{k}_0)]$  has a maximum at  $\mathbf{k}_0$ , which is consistent with that from direct calculations.

We have shown that the giant shift-current and Glass coefficient are directly induced by the nontrivial geometry of the energy band near the valley points. There is no reason that the diverging shift vector is unique to the SnTe monolayer. Experimentally, the giant Glass coefficient is a good sign for the diverging shift-vector. However, the phenomena are best observed when the singular points are at the band edge, where they are isolated. If the singular points are in the middle of the energy bands, the signal may be covered by the light absorption from other  $k$  points.

## CONCLUSIONS

We find a huge shift current effect as well as an enormously large Glass coefficient in the ferroelectric SnTe monolayer. These unusual effects are induced by the non-trivial energy band geometry near the valley points, where the shift-vector diverges. This is another eminent example in which the geometry of the Bloch state plays a profound role in the fundamental properties of a solid. Whereas most previous examples focus on the ground state properties of the solids, this example shows the case of excitation in terms of nonlinear optical transitions, which may have great potential applications in photoelectric devices.

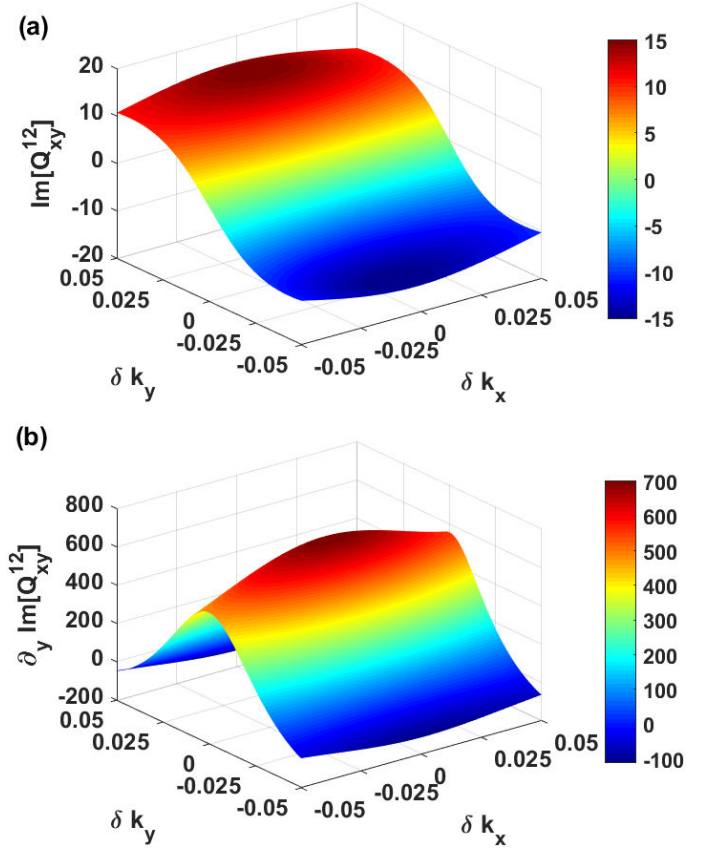


FIG. 4. The distributions of (a)  $\text{Im}[Q_{xy}^{12}]$  and (b)  $\partial_y \text{Im}[Q_{xy}^{12}]$  around the valley point  $\mathbf{k}_0$ .

## METHODS

The first-principles calculations are carried out with the Atomic orbital Based Ab-initio Computation at UStc (ABACUS) code [38, 39] within the Perdew–Burke–Ernzerhof generalized gradient approximation (GGA) for the exchange–correlation functional [40]. The ABACUS code is developed to perform large-scale density functional theory calculations based on numerical atomic orbitals (NAO) [38, 41]. The optimized norm-conserving Vanderbilt (ONCV) [42] fully relativistic pseudopotentials [43] from the PseudoDojo library [44] are used. The valence electrons for Sn, Te are  $4d^{10}5s^25p^2$ , and  $4d^{10}5s^25p^4$ , and the NAO bases for Sn and Te are  $2s2p2d1f$  and  $2s2p2d1f$ , respectively [41].

In the self-consistent and band structure calculations, the energy cut-off for the wave functions is set to 150 Ry. The Brillouin zone is sampled using a  $\Gamma$ -centered  $16 \times 16 \times 1$   $k$ -point mesh. The structure is fully optimized until all forces are less than 1 meV/Å.

After the self-consistent calculations, the tight-binding Hamiltonian,

$$H_{\mu\nu}(\mathbf{R}) = \langle \mathbf{0} | \mu | H | \mathbf{R} \nu \rangle, \quad (16)$$



the overlap matrices,

$$S_{\mu\nu}(\mathbf{R}) = \langle \mathbf{0}\mu | \mathbf{R}\nu \rangle, \quad (17)$$

and the dipole matrices (between the NAOs),

$$\mathbf{r}_{\mu\nu}(\mathbf{R}) = \langle \mathbf{0}\mu | \mathbf{r} | \mathbf{R}\nu \rangle, \quad (18)$$

in the NAO bases are generated, where  $|\mathbf{R}\nu\rangle = \phi_\nu(\mathbf{r} - \tau_\nu - \mathbf{R})$  is the  $\nu$ -th NAO in the  $\mathbf{R}$ -th cell, and  $\tau_\nu$  is the center of the  $\nu$ -th NAO in the unit cell.

The dipole matrix  $r_{nm}^a$  and its generalized derivative  $r_{nm;b}^a$  in the shift current Eq. (5) are calculated as follows [3, 8, 25],

$$r_{nm}^a = \frac{v_{nm}^a}{i\omega_{nm}} \quad (m \neq n), \quad (19)$$

and

$$r_{nm;b}^a = \frac{i}{\omega_{nm}} \left[ \frac{v_{nm}^a \Delta_{nm}^b + v_{nm}^b \Delta_{nm}^a}{\omega_{nm}} - w_{nm}^{ab} + \sum_{p \neq n, m} \left( \frac{v_{np}^a v_{pm}^b}{\omega_{pm}} - \frac{v_{np}^b v_{pm}^a}{\omega_{np}} \right) \right] \quad (m \neq n), \quad (20)$$

where,

$$\begin{aligned} v_{nm}^a &= \frac{1}{\hbar} \langle u_{n\mathbf{k}} | \partial_a H(\mathbf{k}) | u_{m\mathbf{k}} \rangle, \\ \Delta_{nm}^a &= \partial_a \omega_{nm} = v_{nn}^a - v_{mm}^a, \\ w_{nm}^{ab} &= \frac{1}{\hbar} \langle u_{n\mathbf{k}} | \partial_{ab}^2 H(\mathbf{k}) | u_{m\mathbf{k}} \rangle. \end{aligned} \quad (21)$$

The velocity matrix elements  $v_{nm}^a$  are calculated by the *ab initio* tight-binding Hamiltonian Eqs. (16) - (18) [45, 46].

The band structures and the optical properties, such as the shift current are calculated using the tight-binding Hamiltonian implemented in the PY-ATB code [47].

## DATA AVAILABILITY

All data generated and/or analysed during this study are included in this article.

## CODE AVAILABILITY

The ABACUS code is an open source DFT code under the GPL 3.0 licence, which is available from <http://abacus.ustc.edu.cn>. The Py-ATB code, also under the GPL 3.0 licence, can be downloaded from <https://github.com/jingan-181/pyatb>.

## ACKNOWLEDGMENTS

This work was funded by the Chinese National Science Foundation Grant Number 12134012. The numerical calculations were performed on the USTC HPC facilities.

## AUTHOR CONTRIBUTIONS

L. He conducted the project. G. Jin developed the computer code and performed the calculations under the supervision of L. He. Both authors analyzed the results and wrote the manuscript.

## COMPETING INTERESTS

The authors declare no competing interests.

---

\* Corresponding author: helx@ustc.edu.cn

- [1] B. I. Sturman and V. M. Fridkin, *The Photovoltaic and Photorefractive Effects in Noncentrosymmetric Materials* (Gordon and Breach Science Publishers, 1992).
- [2] R. von Baltz and W. Kraut, Theory of the bulk photovoltaic effect in pure crystals, *Phys. Rev. B* **23**, 5590 (1981).
- [3] J. E. Sipe and A. I. Shkrebtii, Second-order optical response in semiconductors, *Phys. Rev. B* **61**, 5337 (2000).
- [4] W. Shockley and H. J. Queisser, Detailed balance limit of efficiency of p-n junction solar cells, *J. Appl. Phys.* **32**, 510 (1961).
- [5] J. E. Spanier, V. M. Fridkin, A. M. Rappe, A. R. Akbashev, A. Polemi, Y. Qi, Z. Gu, S. M. Young, C. J. Hawley, D. Imbrenda, *et al.*, Power conversion efficiency exceeding the shockley-queisser limit in a ferroelectric insulator, *Nat. Photonics* **10**, 611 (2016).
- [6] F. Nastos and J. E. Sipe, Optical rectification and current injection in unbiased semiconductors, *Phys. Rev. B* **82**,

235204 (2010).

- [7] L. Z. Tan, F. Zheng, S. M. Young, F. Wang, S. Liu, and A. M. Rappe, Shift current bulk photovoltaic effect in polar materials—hybrid and oxide perovskites and beyond, *NPJ Comput. Mater.* **2**, 1 (2016).
- [8] A. M. Cook, B. M. Fregoso, F. De Juan, S. Coh, and J. E. Moore, Design principles for shift current photovoltaics, *Nat. Commun.* **8**, 1 (2017).
- [9] A. M. Glass, D. von der Linde, and T. J. Negran, High-voltage bulk photovoltaic effect and the photorefractive process in linbo3, *Appl. Phys. Lett.* **25**, 233 (1974).
- [10] G. Dalba, Y. Soldo, F. Rocca, V. M. Fridkin, and P. Saintavit, Giant bulk photovoltaic effect under linearly polarized x-ray synchrotron radiation, *Phys. Rev. Lett.* **74**, 988 (1995).
- [11] S. Yang, J. Seidel, S. Byrnes, P. Shafer, C.-H. Yang, M. Rossell, P. Yu, Y.-H. Chu, J. Scott, J. Ager, *et al.*, Above-bandgap voltages from ferroelectric photovoltaic devices, *Nat. Nanotechnol.* **5**, 143 (2010).

- [12] M. Alexe and D. Hesse, Tip-enhanced photovoltaic effects in bismuth ferrite, *Nat. Commun.* **2**, 1 (2011).
- [13] A. Bhatnagar, A. Roy Chaudhuri, Y. Heon Kim, D. Hesse, and M. Alexe, Role of domain walls in the abnormal photovoltaic effect in bifeo<sub>3</sub>, *Nat. Commun.* **4**, 1 (2013).
- [14] N. Ogawa, M. Sotome, Y. Kaneko, M. Ogino, and Y. Tokura, Shift current in the ferroelectric semiconductor sbi, *Phys. Rev. B* **96**, 241203 (2017).
- [15] G. B. Osterhoudt, L. K. Diebel, M. J. Gray, X. Yang, J. Stanco, X. Huang, B. Shen, N. Ni, P. J. Moll, Y. Ran, *et al.*, Colossal mid-infrared bulk photovoltaic effect in a type-i weyl semimetal, *Nat. Mater.* **18**, 471 (2019).
- [16] J. Ma, Q. Gu, Y. Liu, J. Lai, P. Yu, X. Zhuo, Z. Liu, J.-H. Chen, J. Feng, and D. Sun, Nonlinear photoresponse of type-ii weyl semimetals, *Nat. Mater.* **18**, 476 (2019).
- [17] J. Ahn, G.-Y. Guo, and N. Nagaosa, Low-frequency divergence and quantum geometry of the bulk photovoltaic effect in topological semimetals, *Phys. Rev. X* **10**, 041041 (2020).
- [18] K. Chang, J. Liu, H. Lin, N. Wang, K. Zhao, A. Zhang, F. Jin, Y. Zhong, X. Hu, W. Duan, *et al.*, Discovery of robust in-plane ferroelectricity in atomic-thick sn<sub>2</sub>e, *Science* **353**, 274 (2016).
- [19] A. Zenkevich, Y. Matveyev, K. Maksimova, R. Gaynutdinov, A. Tolstikhina, and V. Fridkin, Giant bulk photovoltaic effect in thin ferroelectric batio<sub>3</sub> films, *Phys. Rev. B* **90**, 161409 (2014).
- [20] K. Chang, T. P. Kaloni, H. Lin, A. Bedoya-Pinto, A. K. Pandeya, I. Kostanovskiy, K. Zhao, Y. Zhong, X. Hu, Q.-K. Xue, *et al.*, Enhanced spontaneous polarization in ultrathin sn<sub>2</sub>e films with layered antipolar structure, *Adv. Mater.* **31**, 1804428 (2019).
- [21] W. Wan, C. Liu, W. Xiao, and Y. Yao, Promising ferroelectricity in 2d group iv tellurides: a first-principles study, *Appl. Phys. Lett.* **111**, 132904 (2017).
- [22] M. A. U. Absor and F. Ishii, Intrinsic persistent spin helix state in two-dimensional group-iv monochalcogenide *mx* monolayers (*m* = Sn or ge and *x* = S, se, or te), *Phys. Rev. B* **100**, 115104 (2019).
- [23] J. Kim, K.-W. Kim, D. Shin, S.-H. Lee, J. Sinova, N. Park, and H. Jin, Prediction of ferroelectricity-driven berry curvature enabling charge-and spin-controllable photocurrent in tin telluride monolayers, *Nat. Commun.* **10**, 1 (2019).
- [24] S. M. Young and A. M. Rappe, First principles calculation of the shift current photovoltaic effect in ferroelectrics, *Phys. Rev. Lett.* **109**, 116601 (2012).
- [25] J. Ibañez Azpiroz, S. S. Tsirkin, and I. Souza, Ab initio calculation of the shift photocurrent by wannier interpolation, *Phys. Rev. B* **97**, 245143 (2018).
- [26] C. Wang, S. Zhao, X. Guo, X. Ren, B.-L. Gu, Y. Xu, and W. Duan, First-principles calculation of optical responses based on nonorthogonal localized orbitals, *New J. Phys.* **21**, 093001 (2019).
- [27] T. Rangel, B. M. Fregoso, B. S. Mendoza, T. Morimoto, J. E. Moore, and J. B. Neaton, Large bulk photovoltaic effect and spontaneous polarization of single-layer monochalcogenides, *Phys. Rev. Lett.* **119**, 067402 (2017).
- [28] M. Pagliaro, R. Ciriminna, and G. Palmisano, Flexible solar cells, *ChemSusChem* **1**, 880 (2008).
- [29] B. I. Sturman, Ballistic and shift currents in the bulk photovoltaic effect theory, *PHYS-USP+* **63**, 407 (2020).
- [30] J. Jiang, Z. Chen, Y. Hu, Y. Xiang, L. Zhang, Y. Wang, G.-C. Wang, and J. Shi, Flexo-photovoltaic effect in mos<sub>2</sub>, *Nat. Nanotechnol.* **16**, 894 (2021).
- [31] J.-d. Wu, M.-s. Zhao, J.-l. Chen, and Y.-d. Zhang, Adiabatic condition and quantum geometric potential, *Phys. Rev. A* **77**, 062114 (2008).
- [32] T. Morimoto and N. Nagaosa, Topological nature of non-linear optical effects in solids, *Sci. Adv.* **2**, e1501524 (2016).
- [33] N. Nagaosa and T. Morimoto, Concept of quantum geometry in optoelectronic processes in solids: application to solar cells, *Adv. Mater.* **29**, 1603345 (2017).
- [34] B. M. Fregoso, T. Morimoto, and J. E. Moore, Quantitative relationship between polarization differences and the zone-averaged shift photocurrent, *Phys. Rev. B* **96**, 075421 (2017).
- [35] J. Ahn, G.-Y. Guo, N. Nagaosa, and A. Vishwanath, Riemannian geometry of resonant optical responses, *Nat. Phys.* **18**, 290 (2022).
- [36] Y. Gao, Y. Zhang, and D. Xiao, Tunable layer circular photogalvanic effect in twisted bilayers, *Phys. Rev. Lett.* **124**, 077401 (2020).
- [37] H. Watanabe and Y. Yanase, Chiral photocurrent in parity-violating magnet and enhanced response in topological antiferromagnet, *Phys. Rev. X* **11**, 011001 (2021).
- [38] M. Chen, G.-C. Guo, and L. He, Systematically improvable optimized atomic basis sets for ab initio calculations, *J. Phys. Condens. Matter* **22**, 445501 (2010).
- [39] P. Li, X. Liu, M. Chen, P. Lin, X. Ren, L. Lin, C. Yang, and L. He, Large-scale ab initio simulations based on systematically improvable atomic basis, *Comput. Mater. Sci.* **112**, 503 (2016).
- [40] J. P. Perdew, K. Burke, and M. Ernzerhof, Generalized gradient approximation made simple, *Phys. Rev. Lett.* **77**, 3865 (1996).
- [41] P. Lin, X. Ren, and L. He, Strategy for constructing compact numerical atomic orbital basis sets by incorporating the gradients of reference wavefunctions, *Phys. Rev. B* **103**, 235131 (2021).
- [42] D. R. Hamann, Optimized norm-conserving vanderbilt pseudopotentials, *Phys. Rev. B* **88**, 085117 (2013).
- [43] G. Theurich and N. A. Hill, Self-consistent treatment of spin-orbit coupling in solids using relativistic fully separable ab initio pseudopotentials, *Phys. Rev. B* **64**, 073106 (2001).
- [44] M. van Setten, M. Giantomassi, E. Bousquet, M. Verstraete, D. Hamann, X. Gonze, and G.-M. Rignanese, The pseudodojo: Training and grading a 85 element optimized norm-conserving pseudopotential table, *Comput Phys Commun* **226**, 39 (2018).
- [45] C.-C. Lee, Y.-T. Lee, M. Fukuda, and T. Ozaki, Tight-binding calculations of optical matrix elements for conductivity using nonorthogonal atomic orbitals: Anomalous hall conductivity in bcc fe, *Phys. Rev. B* **98**, 115115 (2018).
- [46] G. Jin, D. Zheng, and L. He, Calculation of berry curvature using non-orthogonal atomic orbitals, *J. Phys. Condens. Matter* **33**, 325503 (2021).
- [47] Python ab initio tight binding simulation package (pyatb) (unpublished).